

# High-resolution photoelectron imaging of $\text{MnB}_3^-$ : Probing the bonding between the aromatic $\text{B}_3$ cluster and 3d transition metals

Cite as: J. Chem. Phys. **152**, 244306 (2020); <https://doi.org/10.1063/5.0013355>

Submitted: 10 May 2020 . Accepted: 01 June 2020 . Published Online: 22 June 2020

Ling Fung Cheung , Joseph Czekner , G. Stephen Kocheril , and Lai-Sheng Wang 



View Online



Export Citation



CrossMark

## ARTICLES YOU MAY BE INTERESTED IN

[Photodissociation dynamics of the tert-butyl perthiyl radical](#)

The Journal of Chemical Physics **152**, 244301 (2020); <https://doi.org/10.1063/5.0006913>

[Photodetachment spectroscopy and resonant photoelectron imaging of the 2-naphthoxide anion via dipole-bound excited states](#)

The Journal of Chemical Physics **152**, 214307 (2020); <https://doi.org/10.1063/5.0011234>

[Bound states and symmetry breaking of the ring  \$\text{C}\_{20}^-\$  anion](#)

The Journal of Chemical Physics **152**, 244307 (2020); <https://doi.org/10.1063/5.0012926>

Lock-in Amplifiers  
up to 600 MHz



Watch



# High-resolution photoelectron imaging of $\text{MnB}_3^-$ : Probing the bonding between the aromatic $\text{B}_3$ cluster and 3d transition metals

Cite as: J. Chem. Phys. 152, 244306 (2020); doi: 10.1063/5.0013355

Submitted: 10 May 2020 • Accepted: 1 June 2020 •

Published Online: 22 June 2020



View Online



Export Citation



CrossMark

Ling Fung Cheung,  Joseph Czekner,  G. Stephen Kocheril,  and Lai-Sheng Wang<sup>a)</sup> 

## AFFILIATIONS

Department of Chemistry, Brown University, Providence, Rhode Island 02912, USA

<sup>a)</sup> Author to whom correspondence should be addressed: lai-sheng\_wang@brown.edu

## ABSTRACT

The  $\text{B}_3$  triangular unit is a fundamental bonding motif in all boron compounds and nanostructures. The isolated  $\text{B}_3^-$  cluster has a  $D_{3h}$  structure with double  $\sigma$  and  $\pi$  aromaticity. Here, we report an investigation of the bonding between a  $\text{B}_3$  cluster and a 3d transition metal using high-resolution photoelectron imaging and computational chemistry. Photoelectron spectra of  $\text{MnB}_3^-$  are obtained at six different photon energies, revealing rich vibrational information for the ground state detachment transition. The electron affinity of  $\text{MnB}_3$  is determined to be 1.6756(8) eV, and the most Franck–Condon-active mode observed has a measured frequency of 415(6)  $\text{cm}^{-1}$  due to the Mn– $\text{B}_3$  stretch. Theoretical calculations show that  $\text{MnB}_3^-$  has a  $C_{2v}$  planar structure, with Mn coordinated to one side of the triangular  $\text{B}_3$  unit. The ground states of  $\text{MnB}_3^-$  ( $^6\text{B}_2$ ) and  $\text{MnB}_3$  ( $^5\text{B}_2$ ) are found to have high spin multiplicity with a significant decrease in the Mn–B bond distances in the neutral due to the detachment of an Mn– $\text{B}_3$  anti-bonding electron. The Mn atom is shown to have weak interactions with the  $\text{B}_3$  unit, which maintains its double aromaticity with relatively small structural changes from the bare  $\text{B}_3$  cluster. The bonding in  $\text{MnB}_3$  is compared with that in 5d  $\text{MB}_3$  clusters, where the strong metal– $\text{B}_3$  interactions strongly change the structures and bonding in the  $\text{B}_3$  moiety.

Published under license by AIP Publishing. <https://doi.org/10.1063/5.0013355>

## I. INTRODUCTION

The electron deficiency of boron leads to multi-center delocalized bonding in boron compounds and nanoclusters. The  $\text{B}_3$  triangular unit is the most common bonding motif in planar boron clusters and all three-dimensional (3D) boron polyhedra found in boranes and bulk boron.<sup>1–3</sup> The isolated  $\text{B}_3$  and  $\text{B}_3^-$  species have been well characterized experimentally, and both are known to be equilateral triangles with  $D_{3h}$  symmetry.<sup>4–8</sup> The  $\text{B}_3$  neutral is an open shell with a  $^2\text{A}_1'$  ground state, while the  $\text{B}_3^-$  anion is closed shell ( $^1\text{A}_1'$ ) with double  $\sigma$  and  $\pi$  aromaticity.<sup>5,6</sup> Chemical compounds containing the  $\text{B}_3$  moiety are well known in chemistry.<sup>9–11</sup> However, solid compounds containing isolated aromatic  $\text{B}_3^-$  or  $\text{B}_3^+$  units are not known although there have been theoretical studies.<sup>5,12</sup> In principle,  $\text{B}_3^-$  is the simplest aromatic boron ligand,<sup>13</sup> which can potentially form interesting coordination compounds with transition metals. The viability of  $\text{B}_3^-$  as an

inorganic ligand depends on the strength of its interactions with metal atoms.

Photoelectron spectroscopy (PES) in conjunction with computational chemistry has been shown to be a powerful technique to investigate the structures and bonding of size-selected boron and doped-boron clusters<sup>1,13–16</sup> and provides a unique opportunity to probe the interactions between metals and  $\text{B}_3$ . A number of  $\text{MB}_3^-$  clusters with 5d transition metals have been investigated by combined PES and theoretical studies.<sup>17–20</sup> Of particular interest is the bonding trend of 5d transition metals with the  $\text{B}_3$  cluster. The Ta–B interaction in  $\text{TaB}_3^-$  is strong enough so that the Ta atom breaks the  $\text{B}_3$  ring and forms a fan-like structure.<sup>18</sup> On the other hand, Au has relatively weak interactions with boron, and it behaves like an H atom in its bonding with boron clusters;<sup>21–23</sup> in  $\text{AuB}_3^-$ , the Au atom forms a single Au–B  $\sigma$  bond with one apex of the  $\text{B}_3$  triangle.<sup>17</sup> An intermediate interaction was found in  $\text{IrB}_3^-$ , in which Ir could either have an Ir–( $\eta^2$ - $\text{B}_3$ ) or Ir–( $\eta^3$ - $\text{B}_3$ ) coordination mode,

while the  $B_3$  moiety is distorted relative to the bare  $B_3$  cluster.<sup>19</sup> Recently, the  $ReB_3^-$  cluster was reported to have a quasi-planar structure that is between the fan structure of  $TaB_3^-$  and the  $\eta^3$ -structure of  $IrB_3^-$  with significant distortions to the  $B_3$  unit.<sup>20</sup> There has also been a study of a lanthanide  $B_3$  species ( $PrB_3^-$ ), which was found to have a  $C_{2v}$  planar structure with a  $Pr-(\eta^2-B_3)$  coordination mode.<sup>24</sup> Although the double  $\sigma$  and  $\pi$  aromaticity of the  $B_3$  moiety is maintained in  $PrB_3^-$ , the large atomic size of Pr significantly lengthens the  $B-B$  bond that is coordinated to Pr. In general, the interactions between 5d or 4d transition metals with boron are much stronger than 3d transition metals, as reflected by the superhard 5d borides<sup>25</sup> or the multiple bonds in diatomic MB species.<sup>26,27</sup> The bond energies of 3d diatomic borides are also known to be much weaker than those for 4d or 5d diatomic borides.<sup>28,29</sup> However, there have been no experimental investigations on the  $MB_3^-$  species for 3d transition metals, although there have been theoretical calculations.<sup>30–32</sup>

In the current article, we present a joint PES and theoretical study on  $MnB_3^-$ . We are interested in the coordination modes of Mn to  $B_3$ . Is it side-on [ $Mn-(\eta^2-B_3)$ ] such as in  $PrB_3^-$  or atop [ $Mn-(\eta^3-B_3)$ ] such as in  $ReB_3^-$ ? How much distortion will Mn induce to the  $B_3$  structure? There have been previous studies on larger boron clusters doped with an Mn atom. The  $MnB_{16}^-$  cluster was shown to have a tubular structure with the Mn atom residing in the center of a  $D_{8h}$  boron tube,<sup>33</sup> similar to the  $Co@B_{16}^-$  molecular drum.<sup>34</sup> This study was followed by further theoretical analyses on different 3d transition metal-centered  $B_{16}$  clusters including  $Mn@B_{16}$ .<sup>35,36</sup> A recent study on  $MnB_6$  found that it has a planar structure with a B-centered hexagonal structure and can be viewed as a 3d-metallaboron analog of metallabenzenes.<sup>37</sup> A previous calculation on a series of 3d transition metal doped boron clusters suggested that  $MnB_3$  possesses a  $C_s$  structure, with Mn coordinated to one side of the triangular  $B_3$  unit.<sup>30</sup>

We have carried out a high-resolution PE imaging study on  $MnB_3^-$  and obtained vibrationally resolved PE spectra at six photon energies, which are used to compare with the theoretical calculations to examine the structures, bonding, and vibrational properties of  $MnB_3$ . The structures of  $MnB_3^{-/0}$  are both found to be planar with  $C_{2v}$  symmetry in the  $Mn-(\eta^2-B_3)$  coordination mode. There is a relatively large decrease in the  $Mn-B$  bond lengths in the neutral, due to the detachment of an  $Mn-B_3$  anti-bonding electron. The Mn atom is observed to have weak interactions with boron, in particular, in the anion, and it induces relatively little structural change to the  $B_3$  unit, which maintains its double  $\sigma$  and  $\pi$  aromaticity in  $MnB_3$ . The bonding between Mn and  $B_3$  is compared with that in the  $Ir-(\eta^2-B_3)$  cluster, in which more significant structural changes were found in the  $B_3$  unit due to the strong  $Ir-B$  interactions.<sup>19</sup>

## II. EXPERIMENTAL METHOD

We conducted the experiment using a high-resolution PE imaging apparatus, which has been described in detail previously.<sup>38</sup> Briefly, the second harmonic of a Nd:YAG laser was focused onto a disk target, which was made of a mixture of isotopically enriched  $^{10}B$ , Mn, and Ag powders (the latter was added as a binder). Mn was chosen because it is one of the only two 3d transition metals with a single natural isotope, simplifying the cluster distribution and mass

selection. The laser-induced plasma was cooled by a helium carrier gas seeded with 10% argon, initiating the nucleation process. The clusters were entrained by the carrier gas and underwent a supersonic expansion, generating a cold cluster beam. Anionic clusters were extracted perpendicularly into a time-of-flight mass spectrometer. The  $MnB_3^-$  clusters of interest were mass-selected before entering the interaction zone of a velocity map imaging (VMI) system. A second laser beam from a Deyang Tech dye laser was used to photodetach electrons from the selected  $MnB_3^-$  anions. Photoelectrons were then focused onto a set of microchannel plates coupled with a phosphor screen and a charge-coupled-device camera. A typical experiment required about 50 000–200 000 laser shots to achieve reasonable signal-to-noise ratios. The VMI lens was calibrated using the PE images of  $Au^-$  and  $Bi^-$  at various photon energies. The PE images were analyzed by the maximum entropy method (MEVELER).<sup>39</sup> The typical energy resolution of the VMI detector was  $\sim 0.6\%$  for high kinetic energy electrons and as low as  $1.2 \text{ cm}^{-1}$  for very low energy electrons.<sup>38</sup>

Photoelectron angular distributions (PADs) were obtained from the PE images. PADs can be characterized by an anisotropy parameter ( $\beta$ ). The differential cross section of the photoelectrons is described by

$$d\sigma/d\Omega = \sigma_{\text{Tot}}/4\pi[1 + \beta P_2(\cos\theta)], \quad (1)$$

where  $\sigma_{\text{Tot}}$  is the total cross section,  $P_2$  is the second-order Legendre polynomial, and  $\theta$  is the angle of the photoelectron relative to the laser polarization. The PAD can be described, then, by

$$I(\theta) \sim [1 + \beta P_2(\cos\theta)], \quad (2)$$

where  $\beta$  has a value ranging from  $-1$  to  $2$ . This model works well for single photon transitions from randomly oriented particles. Since photons carry one unit of angular momentum ( $l = \pm 1$ ), the outgoing photoelectrons have the same change in their angular momentum. If an electron is detached from an  $s$  atomic orbital ( $l = 0$ ), the outgoing photoelectron will have  $l = 1$  (pure  $p$ -wave) with  $\beta = 2$ . It is non-trivial to interpret the  $\beta$  value for ionization from a molecular orbital (MO)<sup>40</sup> because MOs are linear combinations of atomic orbitals. Nevertheless, the values of  $\beta$  can be used to qualitatively assess the symmetries of the molecular orbitals involved in the photodetachment process and discern different electronic transitions.

## III. THEORETICAL METHODS

Different structures of  $MnB_3^-$  with various spin multiplicities were calculated at the B3LYP/6-311+G\* level of theory.<sup>41</sup> The adiabatic detachment energy (ADE) for the ground state transition was calculated as the energy difference between the optimized geometry of the anion and that of the neutral. Vibrational analyses were carried out to compare with the experimental data and to ensure that the optimized structures were true minima. Single-point energy calculations were performed at the coupled-cluster single double triple [CCSD(T)] level using the B3LYP geometries.<sup>42</sup> Franck-Condon simulations were performed using the Sharp and Rosenstock method as implemented in PESCAL.<sup>43,44</sup> All calculations were performed using Gaussian 09.<sup>45</sup>

## IV. EXPERIMENTAL RESULTS

The PE images and spectra of  $\text{MnB}_3^-$  at six different photon energies are shown in Fig. 1. The broad vibrational progression suggests a large geometry change from the anion to the neutral. The first peak labeled X represents the transition from the ground state of the anion to that of the neutral. The 0–0 transition yields an accurate electron affinity (EA) for  $\text{MnB}_3$  as  $1.6756 \pm 0.0008$  eV. The major peaks labeled from a to f (Fig. 1 and Table I) define a

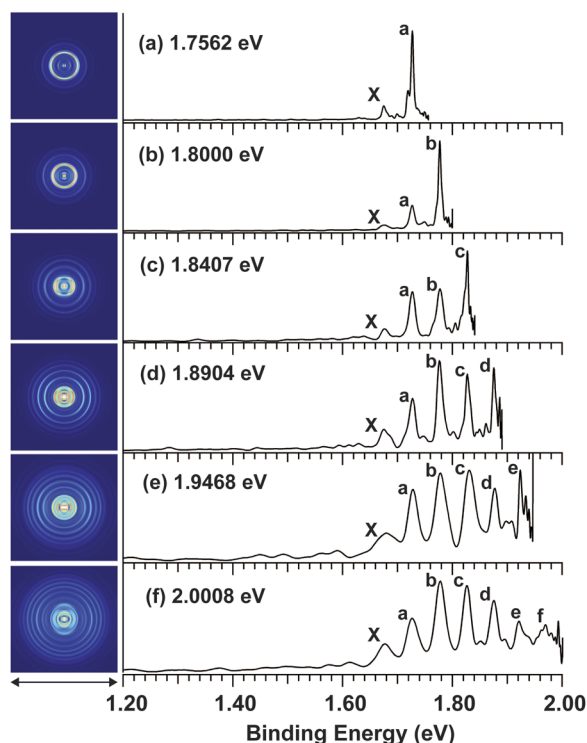


FIG. 1. Photoelectron images and spectra of  $\text{MnB}_3^-$  at six photon energies: (a) 1.7562 eV, (b) 1.8000 eV, (c) 1.8407 eV, (d) 1.8904 eV, (e) 1.9468 eV, and (f) 2.0008 eV. The double arrow below the images indicates the laser polarization.

TABLE I. The binding energies (in eV) of the observed main vibrational peaks in the photoelectron spectra of  $\text{MnB}_3^-$  and their assignments. The energy shift (in  $\text{cm}^{-1}$ ) relative to the peak X is also given.

Peak	Binding energy	Energy shift relative to peak X	Vibrational assignments
X	1.6756(8)	0	$0_0^0$
a	1.7270(3)	415(6)	$3_0^1$
b	1.7771(9)	819(8)	$3_0^2$
c	1.8268(14)	1220(11)	$3_0^3$
d	1.8761(12)	1617(10)	$3_0^4$
e	1.9240(22)	2003(16)	$3_0^5$
f	1.9698(9)	2373(19)	$3_0^6$

vibrational progression with a fundamental frequency of  $415 \text{ cm}^{-1}$ . We also observed numerous weak vibrational peaks (labeled from a' to m' in Fig. S1). The binding energies and assignments of all the observed vibrational features are given in Table S1. The PADs for the major peaks were analyzed, and the obtained values for the anisotropy parameter ( $\beta$ ) at different electron kinetic energies are shown in Fig. S2. The  $\beta$  values were all between 0 and 1.

## V. THEORETICAL RESULTS

The lowest energy structure of  $\text{MnB}_3^-$  was found to be planar with  $C_{2v}$  symmetry and a high spin state ( ${}^6B_2$ ), as shown in Fig. 2. The Mn atom bonds with the  $B_3$  unit in the  $\eta^2$ - $B_3$  coordination mode. The structures of other higher energy isomers are shown in Fig. S3. The closest isomer above the global minimum (0.35 eV) is also a  $C_{2v}$  structure with a quartet spin state ( ${}^4B_2$ ). All other structures are more than 1 eV higher in energy, including the  $\text{Mn}(\eta^1\text{-}B_3)$  coordination isomers (IV–VI in Fig. S2). The fan and tetrahedral structures were all found to have imaginary frequencies. The ground electronic state of  $\text{MnB}_3^-$  has a sextet spin multiplicity ( ${}^6B_2$ ) with a valence electron configuration of  $1a_1^2 2a_1^2 1b_1^2 1b_2^2 2b_2^2 3a_1^2 1a_2^1 4a_1^1 5a_1^1 2b_1^1 6a_1^1$ . The occupied valence molecular orbitals (MOs) of  $\text{MnB}_3^-$  are shown in Fig. 3. Detaching an electron from the  $6a_1$  orbital of  $\text{MnB}_3^-$  yields the neutral ground state of  $\text{MnB}_3$  with a quintet spin multiplicity ( ${}^5B_2$ ). The structure of the neutral ground state is similar to that of the anion, except a significant shortening of the Mn–B bonds by 0.14 Å in the neutral. This bond length change is completely consistent with the nature of the  $6a_1$  singly occupied MO (SOMO) of  $\text{MnB}_3^-$  (Fig. 3), which is mainly of the Mn 4s character with significant antibonding interactions with the  $B_3$  motif. The  $\beta$  values obtained (Fig. S2) are consistent with the nature of the  $6a_1$  SOMO. The calculated EA for  $\text{MnB}_3$  is 1.504 eV at the B3LYP level and 1.744 eV at the CCSD(T) level, which are compared with the experimental value in Table II. Vibrational frequencies were calculated at the B3LYP level for both the anion and neutral  $\text{MnB}_3$ , as shown in Fig. 4.

## VI. DISCUSSION

## A. Comparison of the experimental results with the theoretical calculations

The experimental EA and vibrational frequencies for  $\text{MnB}_3$  are compared with the theoretical values in Table II. The calculated EA

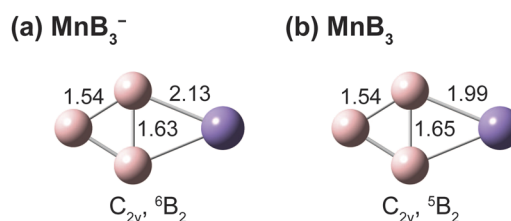


FIG. 2. The global minima of (a)  $\text{MnB}_3^-$  and (b)  $\text{MnB}_3$ . The point group symmetries and electronic states are also given. The bond lengths are given in Å.

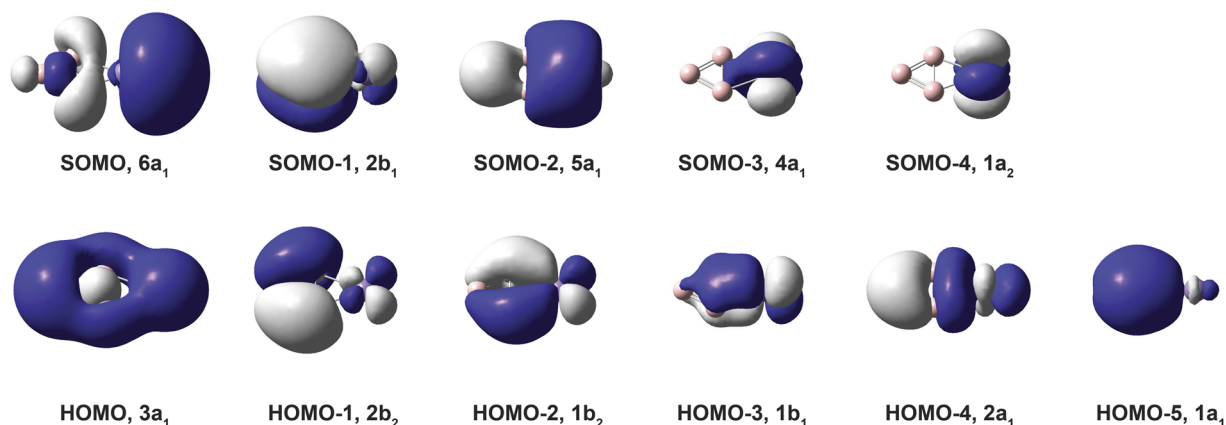


FIG. 3. Occupied valence molecular orbitals of  $\text{MnB}_3^-$  (isovalue = 0.02).

of 1.504 eV at the B3LYP level was underestimated, while the EA of 1.744 eV at the CCSD(T) level agrees well with the experimental value of 1.6756 eV. The main vibrational progression corresponds to the most Franck–Condon-active mode  $\nu_3$ , which involves in the Mn–B<sub>3</sub> stretching (Fig. 4). The computed vibrational frequency of

TABLE II. Comparison of the experimental electron affinity (EA) and vibrational frequencies of  $\text{Mn}^{10}\text{B}_3$  with the theoretical calculations.

	Expt. <sup>a</sup>	B3LYP	CCSD(T)
EA (eV)	1.6756(8)	1.504	1.744
$\nu_1$ ( $\text{cm}^{-1}$ )	1269(7)	1223	
$\nu_3$ ( $\text{cm}^{-1}$ )	415(6)	427	
$\nu_4$ ( $\text{cm}^{-1}$ )	194(8)	194	

<sup>a</sup>The numbers in parentheses represent the uncertainty in the last digit.

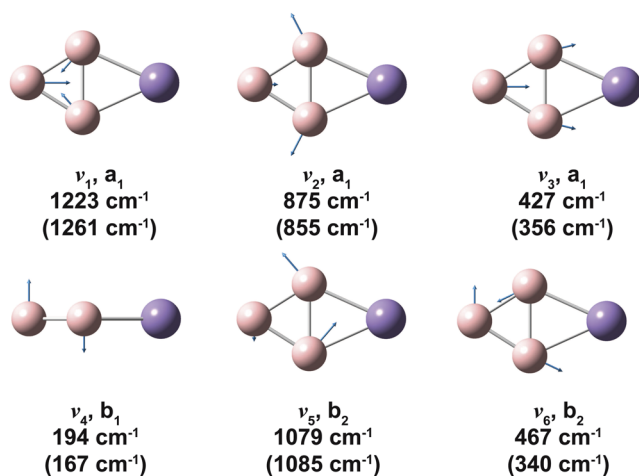


FIG. 4. The displacement vectors and calculated frequencies for all the vibrational modes of  $\text{MnB}_3$ . The calculated frequencies for the anion are given in parentheses.

427  $\text{cm}^{-1}$  for the  $\nu_3$  mode is in good agreement with the observed fundamental frequency of 415  $\text{cm}^{-1}$ . The  $\nu_3$  vibrational progression seems to exhibit a large anharmonicity (Table I). Weak peaks were clearly resolved in between the main vibrational peaks, which were assigned to the bending mode  $\nu_4$  (Fig. 4). However, the  $\nu_4$  bending mode was not symmetry-allowed, and its observation could be due to vibronic coupling. On the other hand, the weak bending vibrational progression seemed to be built off each  $\nu_3$  vibrational peak. This observation could suggest that the  $\text{MnB}_3$  neutral may not be strictly planar. In addition, a weak vibrational feature due to the B<sub>3</sub> breathing mode ( $\nu_1$ , Fig. 4) was also observed (peak e', Fig. S1 and Table S1), which yielded an experimental frequency of 1269  $\text{cm}^{-1}$  for the  $\nu_1$  mode, in good agreement with the computed frequency of 1223  $\text{cm}^{-1}$  (Table II). We have performed a Franck–Condon simulation, as shown in Fig. 5. The main features in the simulated spectrum agree well with the experiment. In the simulation, we fixed the vibrational frequency at 415  $\text{cm}^{-1}$  and then adjusted the anharmonic constant ( $\sim 3 \text{ cm}^{-1}$ ) until a good fit to the experimental data was achieved. Because of the limited accuracy of the measured vibrational spacing, no quantitative information could be obtained for the anharmonicity. Overall, the theoretical results are in good agreement

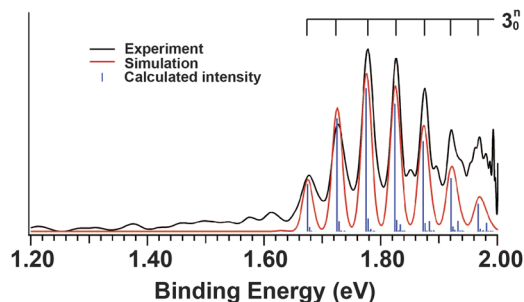


FIG. 5. Franck–Condon simulation for the PES of  $\text{MnB}_3^-$  at 100 K. The vertical lines represent the most active vibrational mode. A vibrational frequency of 415  $\text{cm}^{-1}$  and an anharmonic constant ( $\omega_e X_e$ ) of 3  $\text{cm}^{-1}$  was used for  $\nu_3$ . No other modes were adjusted from the calculations.

with the experimental data, confirming the structures and spin states of the  $\text{MnB}_3^{-/0}$  clusters.

## B. Chemical bonding in $\text{MnB}_3$ and comparison with $\text{IrB}_3$

The 1.54 Å B–B bond length in  $\text{MnB}_3$  is identical to that in bare  $\text{B}_3$  at the B3LYP level.<sup>6</sup> The B–B bond that is coordinated to Mn is only lengthened slightly (1.65 Å), suggesting the relatively weak interaction between Mn and the  $\text{B}_3$  unit. The Mn–B bond length of 2.13 Å in  $\text{MnB}_3^{-}$  is longer than a Mn–B single bond according to Pyykko's single-bond covalent radii (2.04 Å).<sup>46</sup> The Mn–B bonds in neutral  $\text{MnB}_3$  are single bonds upon the removal of the antibonding  $6a_1$  electron (Fig. 3). The previous study on  $\text{IrB}_3^{-}$  found two nearly degenerate structures,  $\text{Ir}-(\eta^2\text{-B}_3)$  ( $C_{2v}$ ) and  $\text{Ir}-(\eta^3\text{-B}_3)$  ( $C_{3v}$ ).<sup>19</sup> The  $C_{2v}$   $\text{IrB}_3$  is similar to  $\text{MnB}_3$ , but the B–B bond lengths are significantly longer (1.623 Å and 1.727 Å) due to the strong Ir–B interactions. In fact, the Ir–B bond lengths (1.872 Å) are even slightly shorter than an Ir=B double bond according to Pyykko's

double-bond covalent radii (1.93 Å).<sup>46</sup> In general, the M–B bonding is strong with 5d transition metals. The M–B bond lengths in the  $\text{TaB}_3^{-}$  fan structure and the 3D  $C_3$   $\text{ReB}_3^{-}$  structure all indicate M=B double bonds.<sup>18,20,46</sup>

We performed AdNDP analyses<sup>47</sup> for the chemical bonding in  $\text{MnB}_3$ , as compared with that of  $\text{Ir}-(\eta^2\text{-B}_3)$  in Fig. 6. We found that the delocalized three-center two-electron (3c-2e)  $\sigma$  and  $\pi$  bonds are intact within the  $\text{B}_3$  unit in  $\text{MnB}_3$  [Fig. 6(a)]. We also found two 2c-2e B–B bonds and two 2c-2e Mn–B bonds, in addition to four localized 3d electrons. It is interesting to see that, in  $\text{Ir}-(\eta^2\text{-B}_3)$ , in addition to two 2c-2e Ir–B bonds, there is a 3c-2e B–Ir–B  $\sigma$  bond and a 3c-2e B–Ir–B  $\pi$  bond, giving rise to the Ir=B double bonds, whereas the 3c  $\sigma$  and  $\pi$  bond in the  $\text{B}_3$  units are both singly occupied, significantly weakening the B–B bonds. On the other hand, the even stronger Ta–B interactions in  $\text{TaB}_3^{-}$  leads to the disruption of the  $\text{B}_3$  triangle, forming the fan structure with three Ta–B bonds.<sup>18</sup> The weak interactions between 3d transition metals and  $\text{B}_3$  lead to the high spin states in  $\text{MnB}_3^{-/0}$ , as well as interesting magnetic properties in bulk 3d metal borides.<sup>48,49</sup>

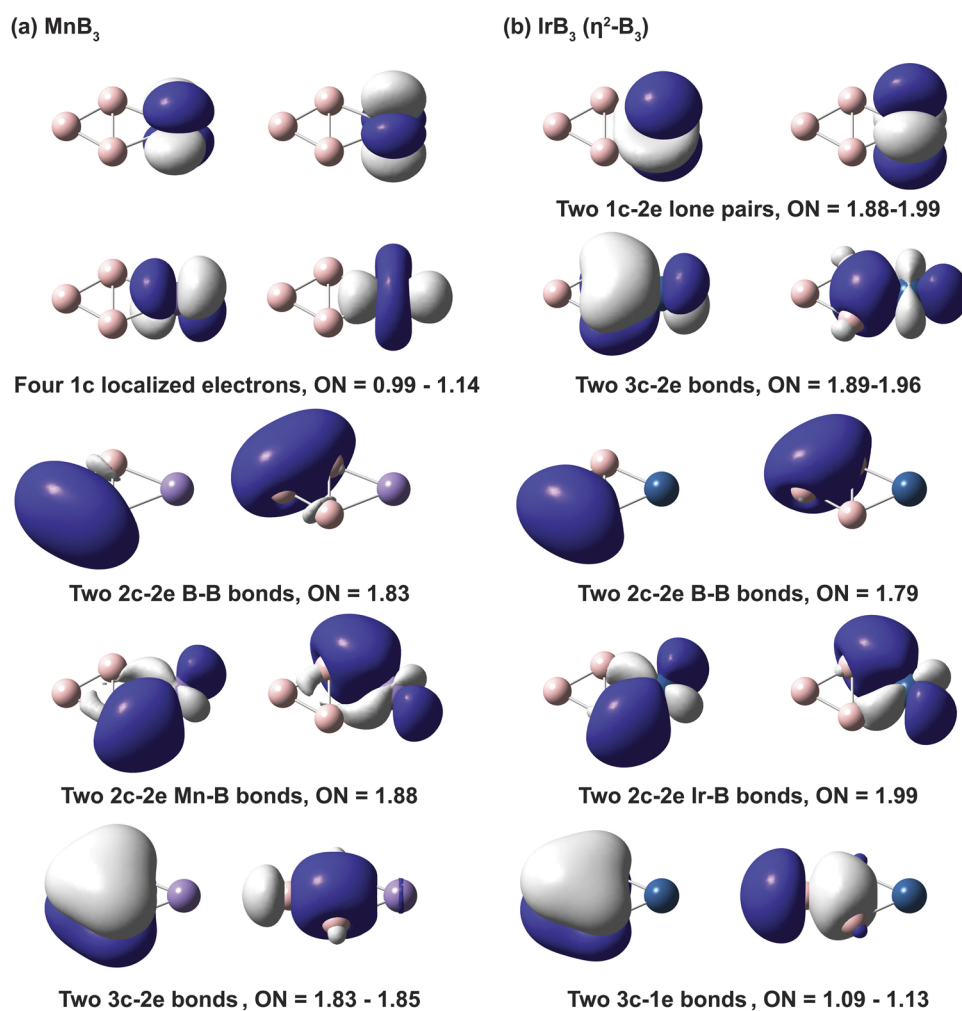


FIG. 6. AdNDP chemical bonding analyses for (a)  $\text{MnB}_3$  and (b)  $\text{IrB}_3$ .

## VII. CONCLUSION

In conclusion, we report an experimental and theoretical investigation of  $\text{MnB}_3^{-/0}$  to probe the interactions between 3d transition metals with the  $\text{B}_3$  cluster. High-resolution photoelectron imaging revealed extensive vibrational information for the ground state photodetachment transition of  $\text{MnB}_3^-$ . The electron affinity of  $\text{MnB}_3$  was measured to be 1.6756(8) eV. Theoretical calculations found that  $\text{MnB}_3^{-/0}$  possesses planar structures with  $C_{2v}$  symmetry, in which Mn is coordinated to  $\text{B}_3$  in an  $\eta^2$ - $\text{B}_3$  fashion. Both  $\text{MnB}_3^-$  ( ${}^6\text{B}_2$ ) and  $\text{MnB}_3$  ( ${}^5\text{B}_2$ ) were found to have high spin states. Three vibrational modes of  $\text{MnB}_3$  were observed in the photoelectron spectra, the most Franck–Condon active  $\nu_3$  mode, the B–B symmetric stretching mode  $\nu_1$ , and the bending mode  $\nu_4$ , with measured frequencies being 415(8), 1269(7), and 194(8)  $\text{cm}^{-1}$ , respectively. Chemical bonding analyses showed that the  $\text{B}_3$  bonding in  $\text{MnB}_3$  is similar to that in bare  $\text{B}_3$ , indicating the relatively weak interactions of  $\text{B}_3$  with Mn. It is shown that, in general, the  $\text{B}_3$  bonding with 3d transition metals is much weaker relative to 5d transition metals.

## SUPPLEMENTARY MATERIAL

See the [supplementary material](#) for the full list of the observed vibrational peaks, anisotropy parameters ( $\beta$ ), and the computed higher energy isomers of  $\text{MnB}_3^-$ .

## ACKNOWLEDGMENTS

This work was supported by the National Science Foundation (Grant No. CHE-1763380).

## DATA AVAILABILITY

The data that support the findings of this study are available from the corresponding author upon reasonable request.

## REFERENCES

- 1 A. P. Sergeeva, I. A. Popov, Z. A. Piazza, W.-L. Li, C. Romanescu, L.-S. Wang, and A. I. Boldyrev, *Acc. Chem. Res.* **47**, 1349–1358 (2014).
- 2 W. N. Lipscomb, *Science* **196**, 1047–1055 (1977).
- 3 B. Albert and H. Hillebrecht, *Angew. Chem., Int. Ed.* **48**, 8640–8668 (2009).
- 4 Y. M. Hamrick, R. J. Van Zee, and W. Weltner, *J. Chem. Phys.* **96**, 1767–1775 (1992).
- 5 A. E. Kuznetsov and A. I. Boldyrev, *Struct. Chem.* **13**, 141–148 (2002).
- 6 H.-J. Zhai, L.-S. Wang, A. N. Alexandrova, A. I. Boldyrev, and V. G. Zakrzewski, *J. Phys. Chem. A* **107**, 9319–9328 (2003).
- 7 M. Wyss, E. Riaplov, A. Batalov, J. P. Maier, T. Weber, W. Meyer, and P. Rosmus, *J. Chem. Phys.* **119**, 9703–9709 (2003).
- 8 Ł. Chacaga, E. B. Jochnowitz, Z. Guennoun, H. Ding, and J. P. Maier, *Int. J. Mass Spectrom.* **280**, 174–178 (2009).
- 9 M. Hofmann and A. Berndt, *Heteroat. Chem.* **17**, 224–237 (2006).
- 10 T. Kupfer, H. Braunschweig, and K. Radacki, *Angew. Chem., Int. Ed.* **54**, 15084–15088 (2015).
- 11 J. Jin, G. Wang, M. Zhou, D. M. Andrada, M. Hermann, and G. Frenking, *Angew. Chem., Int. Ed.* **55**, 2078–2082 (2016).
- 12 L.-m. Yang, J. Wang, Y.-h. Ding, and C.-c. Sun, *J. Phys. Chem. A* **111**, 9122–9129 (2007).
- 13 A. N. Alexandrova, A. I. Boldyrev, H.-J. Zhai, and L.-S. Wang, *Coord. Chem. Rev.* **250**, 2811–2866 (2006).
- 14 L.-S. Wang, *Int. Rev. Phys. Chem.* **35**, 69–142 (2016).
- 15 W. L. Li, X. Chen, T. Jian, T. T. Chen, J. Li, and L. S. Wang, *Natl. Rev. Chem.* **1**, 0071 (2017).
- 16 T. Jian, X. Chen, S.-D. Li, A. I. Boldyrev, J. Li, and L.-S. Wang, *Chem. Soc. Rev.* **48**, 3550–3591 (2019).
- 17 Q. Chen, H. Bai, H.-J. Zhai, S.-D. Li, and L.-S. Wang, *J. Chem. Phys.* **139**, 044308 (2013).
- 18 W.-L. Li, A. S. Ivanov, J. Federič, C. Romanescu, I. Černušák, A. I. Boldyrev, and L.-S. Wang, *J. Chem. Phys.* **139**, 104312 (2013).
- 19 J. Czekner, L. F. Cheung, G. S. Kocheril, M. Kulichenko, A. I. Boldyrev, and L. S. Wang, *Angew. Chem., Int. Ed.* **58**, 8877–8881 (2019).
- 20 L. F. Cheung, G. S. Kocheril, J. Czekner, and L.-S. Wang, *J. Am. Chem. Soc.* **142**, 3356–3360 (2020).
- 21 H.-J. Zhai, L.-S. Wang, D. Y. Zubarev, and A. I. Boldyrev, *J. Phys. Chem. A* **110**, 1689–1693 (2006).
- 22 D. Y. Zubarev, J. Li, L.-S. Wang, and A. I. Boldyrev, *Inorg. Chem.* **45**, 5269–5271 (2006).
- 23 L.-S. Wang, *Phys. Chem. Chem. Phys.* **12**, 8694–8705 (2010).
- 24 X. Chen, T.-T. Chen, W.-L. Li, J.-B. Lu, L.-J. Zhao, T. Jian, H.-S. Hu, L.-S. Wang, and J. Li, *Inorg. Chem.* **58**, 411–418 (2019).
- 25 M. T. Yeung, R. Mohammadi, and R. B. Kaner, *Annu. Rev. Mater. Res.* **46**, 465–485 (2016).
- 26 L. F. Cheung, T.-T. Chen, G. S. Kocheril, W.-J. Chen, J. Czekner, and L.-S. Wang, *J. Phys. Chem. Lett.* **11**, 659–663 (2020).
- 27 L. F. Cheung, G. S. Kocheril, J. Czekner, and L.-S. Wang, *J. Chem. Phys.* **152**, 174301 (2020).
- 28 D. Tzeli and A. Mavridis, *J. Chem. Phys.* **128**, 034309 (2008).
- 29 D. M. Merriles, E. Tieu, and M. D. Morse, *J. Chem. Phys.* **151**, 044302 (2019).
- 30 X. Liu, G. F. Zhao, L. J. Guo, Q. Jing, and Y. H. Luo, *Phys. Rev. A* **75**, 063201 (2007).
- 31 N. M. Tam, L. V. Duong, H. T. Pham, M. T. Nguyen, and M. P. Pham-Ho, *Phys. Chem. Chem. Phys.* **21**, 8365–8375 (2019).
- 32 P. Li, G. Sun, J. Bai, W. Wang, G. Bao, and C. Lu, *New J. Chem.* **41**, 11208–11214 (2017).
- 33 T. Jian, W.-L. Li, I. A. Popov, G. V. Lopez, X. Chen, A. I. Boldyrev, J. Li, and L.-S. Wang, *J. Chem. Phys.* **144**, 154310 (2016).
- 34 I. A. Popov, T. Jian, G. V. Lopez, A. I. Boldyrev, and L. S. Wang, *Nat. Commun.* **6**, 8654 (2015).
- 35 Z. Mahdaviifar and F. Shojaei, *Phys. Chem. Chem. Phys.* **21**, 22618–22628 (2019).
- 36 C.-G. Li, Z.-G. Shen, J. Zhang, Y.-Q. Cui, J.-J. Li, H.-Y. Xue, H.-F. Li, B.-Z. Ren, and Y.-F. Hu, *New J. Chem.* **44**, 5109–5119 (2020).
- 37 L. F. Cheung, G. S. Kocheril, J. Czekner, and L.-S. Wang, *J. Phys. Chem. A* **124**, 2820–2825 (2020).
- 38 I. León, Z. Yang, H.-T. Liu, and L.-S. Wang, *Rev. Sci. Instrum.* **85**, 083106 (2014).
- 39 B. Dick, *Phys. Chem. Chem. Phys.* **16**, 570–580 (2014).
- 40 A. Sanov and R. Mabbs, *Int. Rev. Phys. Chem.* **27**, 53–85 (2008).
- 41 A. D. Becke, *J. Chem. Phys.* **98**, 5648–5652 (1993).
- 42 J. A. Pople, M. Head-Gordon, and K. Raghavachari, *J. Chem. Phys.* **87**, 5968–5975 (1987).
- 43 T. E. Sharp and H. M. Rosenstock, *J. Chem. Phys.* **41**, 3453–3463 (1964).
- 44 K. M. Ervin, PESCAL, Fortran program, 2010.
- 45 M. J. Frisch, G. W. Trucks, H. B. Schlegel, G. E. Scuseria, M. A. Robb, J. R. Cheeseman, G. Scalmani, V. Barone, B. Mennucci, G. A. Petersson, H. Nakatsuji, M. Caricato, X. Li, H. P. Hratchian, A. F. Izmaylov, J. Bloino, G. Zheng, J. L. Sonnenberg, M. Hada, M. Ehara, K. Toyota, R. Fukuda, J. Hasegawa, M. Ishida, T. Nakajima, Y. Honda, O. Kitao, H. Nakai, T. Vreven, J. A. Montgomery, Jr., J. E. Peralta, F. Ogliaro, M. Bearpark, J. J. Heyd, E. Brothers, K. N. Kudin, V. N. Staroverov, R. Kobayashi, J. Normand, K. Raghavachari, A. Rendell, J. C. Burant, S. S. Iyengar, J. Tomasi, M. Cossi, N. Rega, J. M. Millam, M. Klene,

J. E. Knox, J. B. Cross, V. Bakken, C. Adamo, J. Jaramillo, R. Gomperts, R. E. Stratmann, O. Yazyev, A. J. Austin, R. Cammi, C. Pomelli, J. W. Ochterski, R. L. Martin, K. Morokuma, V. G. Zakrzewski, G. A. Voth, P. Salvador, J. J. Dannenberg, S. Dapprich, A. D. Daniels, Ö. Farkas, J. B. Foresman, J. V. Ortiz, J. Cioslowski, and D. J. Fox, Gaussian 09, Revision C.1, Gaussian, Inc., Wallingford, CT, 2009.

<sup>46</sup>P. Pyykkö, *J. Phys. Chem. A* **119**, 2326–2337 (2015).

<sup>47</sup>D. Y. Zubarev and A. I. Boldyrev, *Phys. Chem. Chem. Phys.* **10**, 5207–5217 (2008).

<sup>48</sup>H. Gou, A. A. Tsirlin, E. Bykova, A. M. Abakumov, G. Van Tendeloo, A. Richter, S. V. Ovsyannikov, A. V. Kurnosov, D. M. Trots, Z. Konôpková, H.-P. Liermann, L. Dubrovinsky, and N. Dubrovinskaia, *Phys. Rev. B* **89**, 064108 (2014).

<sup>49</sup>J. P. Scheifers, Y. Zhang, and B. P. T. Fokwa, *Acc. Chem. Res.* **50**, 2317–2325 (2017).